Journal of Power Sources 631 (2025) 236227

Contents lists available at ScienceDirect

Journal of Power Sources

journal homepage: www.elsevier.com/locate/jpowsour

Effect of Ti doping on properties of TiN/(Ta, Ti)N coated TC4 bipolar plate in proton exchange membrane fuel cells environment

Wei Li [a,*], Yong Wang [a], Xiulan Li [a], Xinjun Zhou [a], Xiao Jiang [a], Can Xiong [a], Yao Chen [a], Fei You [a], Zhengyu Guo [a], Yuan Zhang [a], Lintao Liu [b], Xuan Li [a]

[a] Faculty of Mechanical Engineering, Sichuan University of Science & Engineering, Yibin, 644000, China
[b] Northwest Institute for Nonferrous Metals Research, China

HIGHLIGHTS

- The Ti/TiN/(Ta, Ti)N coating was deposited on TC4 though magnetron sputtering.
- The effects of Ti doping on coating structure and phase evolution were explored.
- The mechanisms of conductive and corrosion resistant in coatings were discussed.
- Trace Ti doping (60W) reduced coating porosity significantly, from 0.99 % to 0.38 %.

GRAPHICAL ABSTRACT

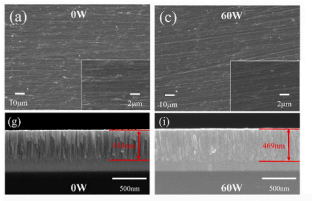

SEM microstructure of coatings under 0W and 60W

ICR values of the coating samples before and after corrosion at a compaction force of 140 N/cm²

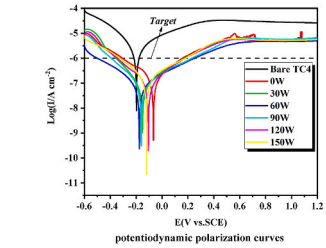

potentiodynamic polarization curves

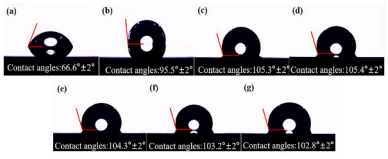

Water contact angle of the samples: (a) Bare TC4. (b) 0 W. (c) 30 W. (d) 60 W. (e) 90 W. (f) 120 W. (g) 150 W.

ARTICLE INFO

Keywords:
PEMFC
TC4 bipolar plate
(Ta, Ti)N
Corrosion resistance
Conductivity

ABSTRACT

To address the issues of inadequate corrosion resistance and electrical conductivity in titanium-based bipolar plates under the proton exchange membrane fuel cell (PEMFC) environment, Ti/TiN/(Ta, Ti)N multilayer coatings are deposited on TC4 bipolar plates using magnetron sputtering technology. This multilayer coating structure consists of a Ti bonding layer, a TiN transition layer, and a Ti-doped TaN outer layer. The Ti content in the (Ta, Ti)N layer is adjusted by altering the Ti target power, and its effect on the microstructure and performance of the coating is systematically evaluated. Results show that lower Ti target power suppresses columnar crystal growth in the (Ta, Ti)N layer, reducing the grain size and porosity of the coatings, which significantly enhances the coating's corrosion resistance. The coating exhibits optimal corrosion resistance at a Ti target power of 60 W. During potentiostatic polarization at 0.6 V and 1.2 V (vs. SCE), the Ti/TiN/(Ta, Ti)N-60W coating demonstrates corrosion current densities as low as 8.98×10^{-8} A/cm^2 and 9.41×10^{-7} A/cm^2, respectively. Moreover, the increase in Ti target power promotes the formation of the highly conductive TiN phase in the (Ta,

* Corresponding author.
E-mail address: liweibuqi@163.com (W. Li).

https://doi.org/10.1016/j.jpowsour.2025.236227
Received 30 December 2024; Received in revised form 9 January 2025; Accepted 11 January 2025
Available online 18 January 2025

Ti)N layer, lowering the interfacial contact resistance (ICR) from 6.85 mΩ cm^2 to 4.22 mΩ cm^2 at a compaction force of 140 N/cm^2. These findings underscore the potential of Ti/TiN/(Ta, Ti)N multilayer coatings as promising functional materials for PEMFC bipolar plates, achieving a balance between superior corrosion resistance and enhanced electrical conductivity.

1. Introduction

Hydrogen energy, recognized as a favorable alternative to fossil fuels due to its non-polluting nature and diverse sources, has garnered extensive attention from energy researchers worldwide [1]. As a fifth-generation fuel cell technology, proton exchange membrane fuel cells (PEMFC) are characterized by compact design, low operating temperatures, and high energy conversion efficiencies ranging from 40 % to 60 %, making them essential tools for hydrogen energy conversion [2,3]. As a critical component of the PEMFC system, the bipolar plate constitutes approximately 80 % of the total mass and 30 % of the overall cost of the fuel cell stack [4]. Its functions include gas dispersion, conduction current collection, and series connection of individual cells, all of which significantly influence the performance and lifespan of the fuel cell [5,6]. To ensure effective operation of the PEMFC, the bipolar plate must exhibit excellent electrical, thermal, corrosion, and gas tightness, along with robust mechanical properties [7]. According to the 2025 performance standards proposed by the U.S. Department of Energy (DOE) for bipolar plates, the corrosion current density must be below 1 $\times$ 10^{-6} A/cm^2 in a 0.6 V (vs. SHE) cathode environment, and the interfacial contact resistance (ICR) must not exceed 10 mΩ cm^2 under a compaction force of 140 N/cm^2 [8]. Presently, there are three primary types of bipolar plate materials: graphite, composite materials, and metal [9–11]. Among these, metal bipolar plates offer good toughness, high strength, and excellent thermal and electrical conductivity, making them more promising choices for bipolar plate materials [12]. Currently, metal bipolar plate substrates can be categorized into three types: titanium alloys, stainless steel, and aluminum alloys [13–17]. However, when stainless steel undergoes corrosion in the PEMFC environment, it releases various harmful metal cations (Fe^{3+}, Cr^{3+}, Ni^{2+}) into the electrolyte, accelerating the degradation of the membrane electrode assembly (MEA). Additionally, aluminum alloys exhibit even poorer corrosion resistance in the PEMFC environment, with a corrosion rate nearly ten times higher than that of stainless steel. Furthermore, aluminum alloys readily form passivation films on their surfaces, significantly compromising the service life and output efficiency of PEMFCs [13–15]. Compared to the other two metals, due to titanium alloy excellent corrosion resistance, favorable mechanical properties, and the low toxicity of titanium ions released in the PEMFC environment, which has minimal impact on the MEA, its has increasingly become the preferred material for metal bipolar plate substrates [16,17]. However, the MEA generates F^- during the operation of the PEMFC, leading to some degree of corrosion of the titanium bipolar plate. Furthermore, the passive films that spontaneously form in the PEMFC environment increase the ICR of the titanium bipolar plate, significantly reducing the output efficiency and lifespan of the PEMFC [18].

To address this issue, the most commonly used approach is to modify the surface of the titanium bipolar plate by applying a coating that enhances its corrosion resistance and conductivity in the PEMFC environment. These coatings encompass precious metal coatings [19,20], oxide coatings [21], carbon-based coatings [22,23], transition metal-carbon/nitride coatings [4,24], and polymer coatings [25]. Among these, transition metal nitride coatings exhibit excellent corrosion resistance, high conductivity, low cost, and ease of fabrication, making them widely utilized as protective coatings for metal bipolar plates. The primary preparation method is physical vapor deposition (PVD), which offers higher deposition efficiency and lower costs compared to other technologies [26,27]. Notably, the thermal expansion coefficients of TiN and titanium exhibit minimal differences (0.63 %), promoting enhanced adhesion between the TiN coating and the titanium bipolar plate. Furthermore, TiN demonstrates high electrical conductivity (4.55 $\times$ 10^6 S/m), establishing it as an ideal coating material for titanium bipolar plates [28–30]. Yan et al. [31] prepared TiN coatings optimally oriented along the (111) crystal plane on titanium surfaces through reactive magnetron sputtering, achieving an ICR value of only 1.9 mΩ cm^2 and a low corrosion current density of 9.1 $\times$ 10^{-7} A/cm^2. Additionally, TaN coatings exhibit excellent thermal stability, corrosion resistance, and a broader passivation potential range in the PEMFC environment, making them an increasingly preferred choice for metal bipolar plate coatings. Choe et al. [32] employed reactive magnetron sputtering to fabricate TaNx coatings on AISI 316L substrates, and the coatings exhibited a corrosion current density as low as 3.33 $\times$ 10^{-7} A/cm^2 at 0.6 V (vs. SHE), demonstrating exceptional corrosion resistance. However, single-layer metal nitride coatings prepared by PVD often exhibit numerous defects, including pinholes, large particles, and columnar crystal structures. The corrosive medium can easily penetrate the coating through these defects, leading to localized corrosion and potentially causing the coating to detach. Research indicates that doping metal or non-metal elements into a single metal nitride coating to create a multi-component coating structure can effectively prevent the formation of these defects [33–36]. Jin et al. [33] utilized unbalanced magnetron sputtering to fabricate TiAlN coatings with varying Al target currents on an SS316L substrate. The results indicate that introducing the Al element effectively inhibits the typical growth trend of TiN's columnar crystal structure. When the deposition current of the Al target is 2 A, the coating exhibits optimal corrosion resistance. Similarly, Bi et al. [34] employed magnetron sputtering technology to dope Al elements into a CrN coating, finding that the introduction of Al refined the grain size of CrN, resulting in improved corrosion resistance of the CrN coating. However, while doping elements into the single-layer nitride coating can inhibit the formation of columnar crystal structures and pinholes, the single-layer doped coating still poses a risk of failure under the harsh operating conditions of PEMFC. Mani et al. [37] compared the corrosion resistance of CrN/CrAlN, CrN, and CrAlN coatings in the HT-PEMFC environment, finding that the CrN/CrAlN coating exhibited the best corrosion resistance, with a protection efficiency of up to 98.12 %. Wu et al. [38] designed a TiN/TiCN multilayer coating with a thickness of 2 μm. The coating possesses a dense structure, and the corrosion current density is only 1.2 $\times$ 10^{-7} A/cm^2.

The analysis presented above indicates that multilayer doped coatings exhibit superior performance compared to single nitride coatings or single-doped coatings in the PEMFC environment. Consequently, this study aims to design a multilayer doped coating with a similar structure and evaluate its feasibility for titanium bipolar plate applications. It is well-established that TaN and TiN share analogous NaCl structures, and their lattice constants are very similar, allowing for the mutual substitution of metal atoms between the two phases. The complete miscibility of the TaN and TiN phases can be achieved by doping Ti into the TaN coating, resulting in the generate of a stable (Ta, Ti)N ternary solid solution phase [39,40]. Unfortunately, research on doping Ti into TaN coatings has primarily focused on wear resistance and hardness, with limited studies addressing its application in metal bipolar plate coatings. Therefore, in this study, magnetron sputtering were employed to deposit a Ti/TiN/(Ta, Ti)N multilayer composite coating on the TC4 substrate. This coating consisted of a Ti bonding layer, a TiN transition layer with superior conductivity, and a Ti-doped (Ta, Ti)N top layer exhibiting excellent corrosion resistance and conductivity. The influence of varying Ti target power on the microstructure, phase composition, and

properties of the Ti/TiN/(Ta, Ti)N coating was systematically investigated.

2. Experimental methods

2.1. Coating preparation

The experimental substrates used in this study were TC4 titanium alloy (Ti-6Al-4V) samples with dimensions of 15 mm × 15 mm × 1 mm, and single-crystal silicon wafers (001) measuring 10 mm × 10 mm × 0.5 mm. To ensure a high-quality deposition interface, the substrates were sequentially ground to a mirror finish using SiC sandpaper, followed by polishing with 0.5 μm diamond paste. The substrates were then ultrasonically cleaned in a mixed solution of acetone and alcohol. Finally, the polished samples were rinsed with distilled water and dried in a bellows for subsequent use.

In this experiment, thin film deposition was carried out using a high-vacuum multi-target magnetron sputtering system. A DC Ta target (99.999 %) and an RF Ti target (99.999 %) were installed in the coating chamber. Prior to initiating the coating process, the chamber vacuum was required to reach 1.5×10^{-3} Pa, the temperature was set to 300 °C, the bias voltage was adjusted to −50 V, and the sample holder was rotated at a constant speed of 8 r/min to ensure uniform deposition across the sample surface. During the deposition of the Ti bonding layer and TiN transition layer, the Ti target power was set to 200 W and 150 W, respectively, with deposition times of 15 min and 60 min. For the deposition of the (Ta, Ti)N layer, the DC Ta target current was maintained at 0.3 A, while the RF Ti target power was adjusted in 30 W increments, varying the Ti target power between 0 W and 150 W to complete over a period of 90 min. Throughout the deposition of both the TiN and (Ta, Ti)N layers, the mass flow rates of Ar and N_2 were consistently set at 17.5 sccm and 7.5 sccm, respectively. A detailed

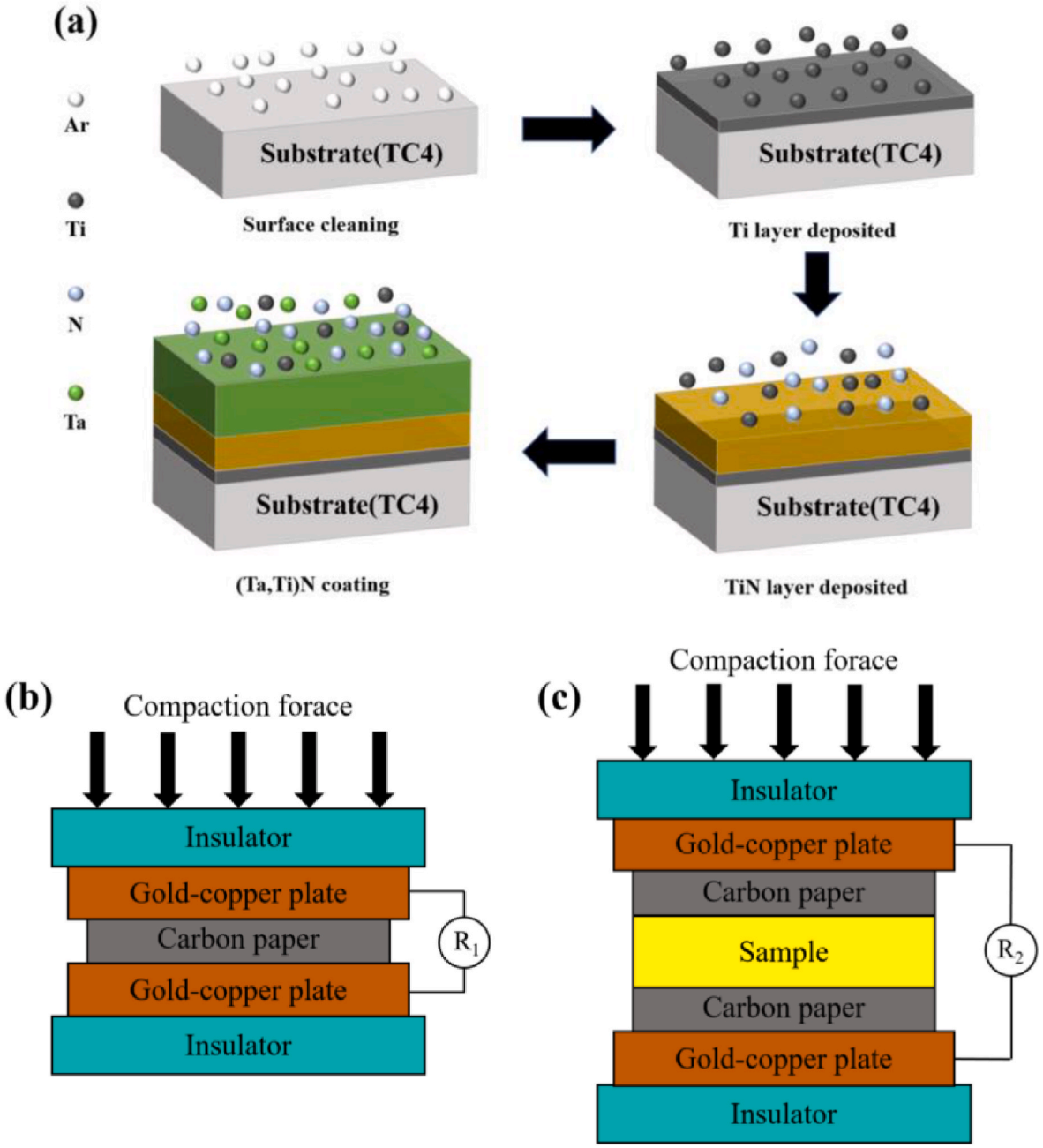

Fig. 1. (a) Flowchart of the coating preparation process. (b) Schematic diagram of R_1 test for the samples. (c) Schematic diagram of R_2 test for the samples.

schematic of the coating preparation process is presented in Fig. 1a.

2.2. Microscopic characterization

The microstructure of the multilayer composite coating were examined using a VEGA3 SUB scanning electron microscope (SEM) operating at 15 kV. The phase composition was analyzed via a D2 PHASER X-ray diffractometer (XRD), with data recorded across a diffraction angle range of 10°–90° at a scanning speed of 11.43°/min. The chemical states of elements in the (Ta, Ti)N layer were investigated using a Thermo Fisher Scientific X-ray photoelectron spectrometer (XPS), equipped with an Al Kα radiation source emitting at 1486.76 eV.

2.3. Electrochemical tests

The corrosion resistance of the coating was assessed using the MFT-EC4000 friction and wear testing apparatus manufactured by Huahui Company. A three-electrode configuration was adopted, where a platinum electrode was used as the counter electrode, a saturated calomel electrode (SCE) served as the reference electrode, and the coating sample or TC4 substrate acted as the working electrode. The sample's exposed working area measured 1 cm^2. The corrosion medium comprised 0.5 mMol/L H_2SO_4 and 5 mg/L HF, with air bubbling introduced under heating at 80 °C in a water bath. Before initiating the test, the system was stabilized for 30 min. Potentiodynamic polarization measurements were carried out within a potential range of −0.6 V–1.2 V (vs. SCE) over a 30-min duration. Additionally, potentiostatic polarization testing was conducted at 0.6 V and 1.2 V (vs. SCE) for 7200 s and 3600 s, respectively. Electrochemical impedance spectroscopy (EIS) analysis covered frequencies from 10^5 Hz to 10^{-2} Hz, with a 10 mV amplitude and a measurement period of 1440 s.

2.4. Interfacial contact resistance (ICR) and hydrophobicity tests

In this study, the ICR values of the samples were determined using the procedure described by Kumar [41]. The method involves positioning the sample between two carbon paper sheets (YLS-35, TORAY, Japan) to simulate the contact resistance occurring between the bipolar plate and the diffusion layer. To reduce measurement errors, the opposite side of the carbon paper makes contact with a gold-plated copper plate. The current is maintained constant, and a pressure ranging from 20 N/cm^2 to 200 N/cm^2 is applied to the test sample by a universal testing machine. The resistance values under different pressures are then recorded. To ensure data reliability, each sample was measured three times and the average value was taken. Finally, the resistance values obtained from the measurements are substituted into the specified formula to calculate the ICR value of the sample [21,22]. Fig. 1b shows the test schematic diagram of the total resistance (R_1) of the system when no sample is placed, with the following formula relationship:

$$R_1 = 2\,R_{cu} + R_{cp} + 2\,R_{cu/cp} \tag{1}$$

Here, R_{cu} represents the resistance value of the gold-plated copper plate, R_{cp} represents the resistance value of the carbon paper, and $R_{cu/cp}$ represents the contact resistance between the gold-plated copper plate and the carbon paper. Fig. 1c shows the test schematic diagram of the total system resistance (R_2) after placing the sample, with the following formula relationship:

$$R_2 = 2\,R_{cu} + 2\,R_{cp} + 2\,R_{cp/sam} + R_{sam} + 2\,R_{cu/cp} \tag{2}$$

here, R_{sam} represents the resistance of the sample itself, while $R_{cp/sam}$ is the contact resistance between the carbon paper and the sample. Therefore, $R_{cp/sam}$ can be obtained using the following formula:

$$R_2 - R_1 = 2\,R_{cp/sam} + R_{sam} + R_{cp} \tag{3}$$

Since the resistance of the TC4 substrate and carbon paper itself is much smaller than the total resistance R_2, it can be neglected in the calculation, allowing the following simplified formula:

$$R_{cp/sam} = 0.5\,(R_2 - R_1) \tag{4}$$

Finally, the calculated $R_{gdl/sam}$ value is multiplied by the contact area (A) between the sample and the carbon paper to determine the ICR value of the sample:

$$ICR = R_{cp/sam} \times A \tag{5}$$

The hydrophobicity of the samples was evaluated with a contact angle tester (model JC2000C). Measurements were conducted at three randomly chosen points on the sample surface, and the water contact angles were recorded. For accuracy, the average of these three measurements was used as the final water contact angle of the sample.

3. Results and discussion

3.1. Morphology of coatings

Fig. 2 presents the SEM images showcasing the surface and cross-sectional microstructures of the coating samples. From the surface topography (Fig. 2a–f), it is evident that the coating surface becomes smooth and dense with a small amount of Ti doping, and no significant defects such as holes are observed. However, when the Ti target power exceeds 60 W, the porosity of the coating surface increases. This increase is attributed to the higher Ti target power, which introduces more stresses and defects, subsequently raising the defect density of the coating. From the cross-sectional morphology (Fig. 2g–l), each film appears continuous, dense, and well-bonded to the interface. Because of the brief deposition duration of the Ti seed layer, only the TiN and (Ta, Ti)N layers are visible in the cross-sectional images. Under undoped conditions, the TaN layer reveals a characteristic columnar crystal morphology, while TiN layer displays a dense and uniform structure, reflecting the differing deposition characteristics of DC and RF magnetron sputtering. As the Ti target power increases, the density of the cross-sectional columnar structure of the (Ta, Ti)N layer gradually increases, while the morphology of the columnar crystalline structure diminishes, with the suppression of the columnar crystal structure being most pronounced at a Ti target power of 60 W. Conversely, after exceeding 60 W, the columnar crystal structure of the (Ta, Ti)N layer becomes more pronounced. This occurs because, at higher Ti target power, excessive accumulation of the TiN phase in the (Ta, Ti)N layer causes the coating grains to grow perpendicular to the substrate, resulting in a more pronounced columnar crystal structure. Thus, trace amounts of Ti can effectively reduce the surface roughness of the coating and weaken the columnar crystal structure of the (Ta, Ti)N layer, thereby increasing the compactness of the coating. However, excessive Ti leads to an increase in surface pores and promotes the growth of thick columnar crystals. Furthermore, the thickness of the (Ta, Ti)N layer initially increases from 414 nm (0 W) to 469 nm (60 W) before decreasing to 322 nm (150 W) as the Ti target power rises. This behavior is due to increased collisions between Ti and Ta particles at higher power, resulting in fewer particles being deposited on the substrate and a reduced growth rate of the coating [39].

3.2. Phase composition

Fig. 3a presents the XRD spectra of different Ti/TiN/(Ta, Ti)N coatings. Owing to the comparable lattice parameters of TiN and TaN, their diffraction peaks exhibit significant overlap. Apart from the diffraction peaks observed at 2θ angles of approximately 35.5°, 41.5°, 60°, and 76°, all other peaks originate from the TC4 substrate. Upon doping with Ti in the TaN layer, the diffraction peak corresponding to the (200) crystal plane disappears, while the peak for the (111) crystal

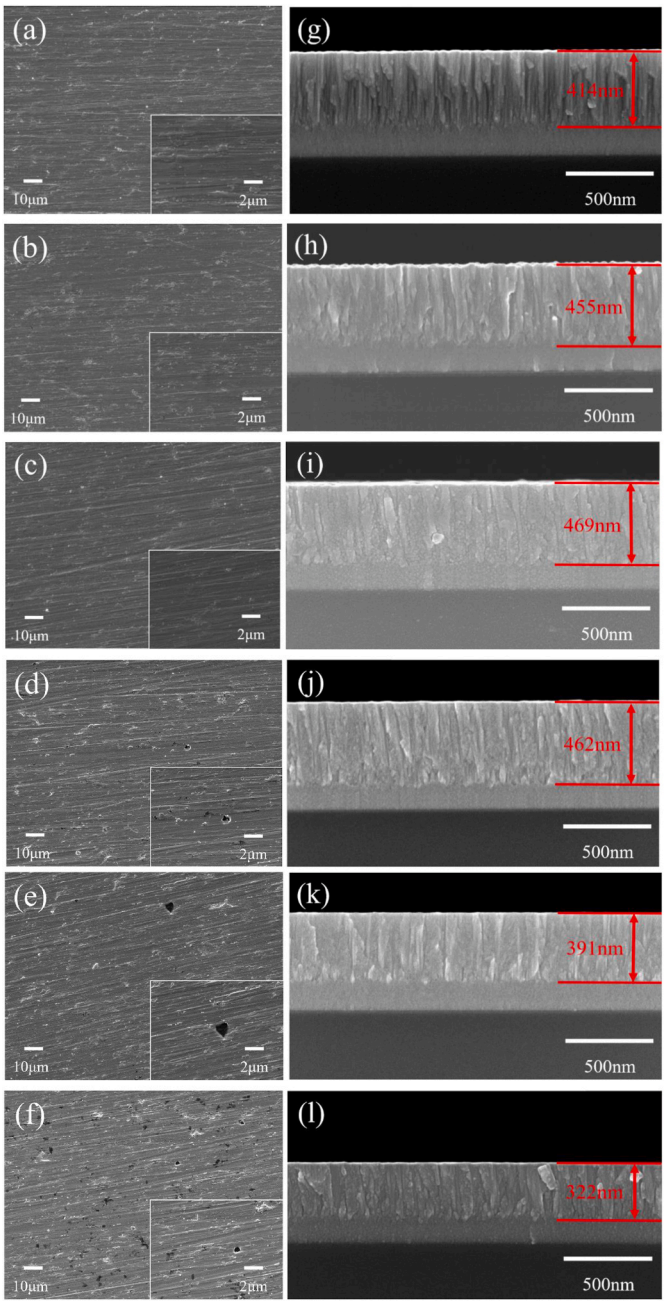

Fig. 2. SEM microstructure of coatings under different Ti target powers: (a, g) 0 W. (b, h) 30 W. (c, i) 60 W. (d, j) 90 W. (e, k) 120 W. (f, l) 150 W.

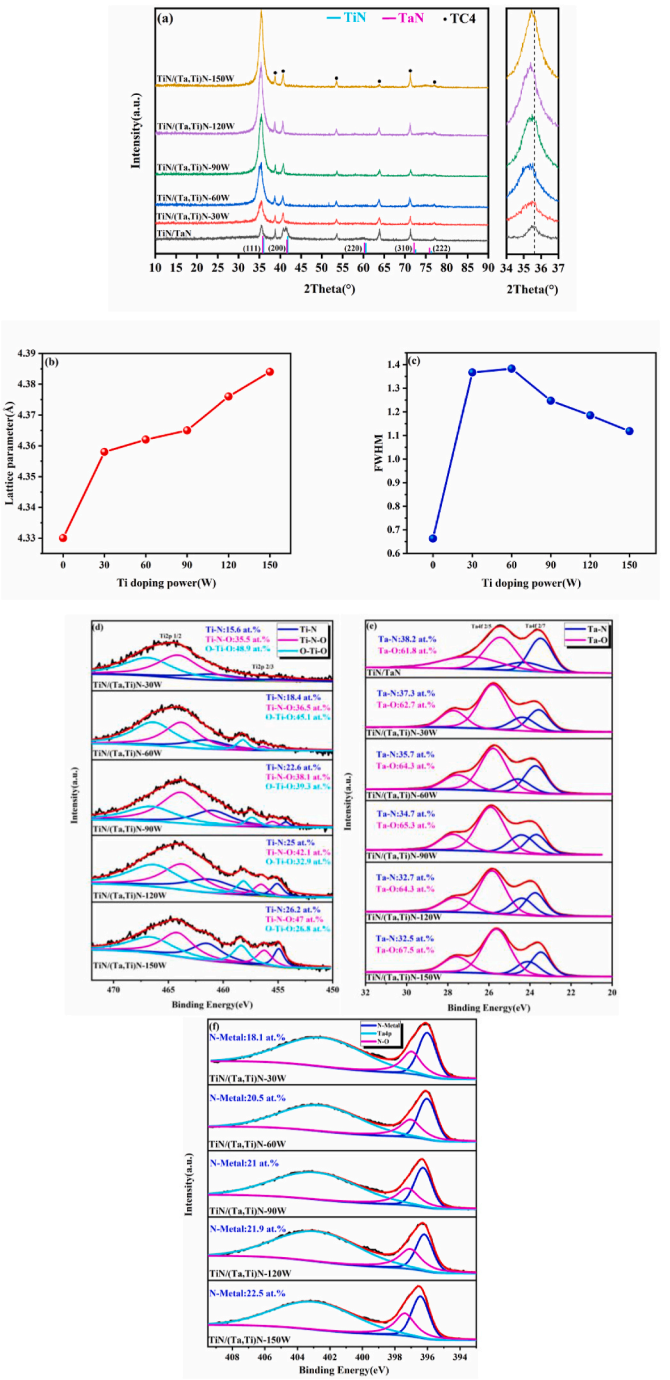

Fig. 3. (a) XRD comparison of samples. (b) lattice parameter change of samples. (c) variation of the full width of half peaks of samples. (d) XPS spectrum of Ti2p. (e) XPS spectrum of Ta4f. (f) XPS spectrum of N1s.

plane is enhanced with increasing Ti target power. This observation indicates the formation of a ternary solid solution phase (Ta, Ti)N with a rock salt structure [42,43]. Furthermore, the intensity of the (111) crystal plane's diffraction peak is significantly stronger than that of other crystal planes, suggesting that the (Ta, Ti)N phase preferentially grows along the (111) direction, which can be attributed to the lowest strain energy associated with this plane. It is worth noting that the diffraction peak of the (111) crystal plane gradually shifts to a lower 2θ angle with the Ti target power rises. This shift may result from the replacement of Ta atoms by Ti atoms in the TaN lattice, causing local distortion and stress accumulation. To relieve this stress, the lattice slightly expands, leading to a low-angle shift of the diffraction peak [44,45]. To confirm this conclusion, the lattice parameters of the coating samples were calculated using the Bragg equation: $2d\sin\theta = \lambda$, based on the (111) and (200) peak positions from the XRD patterns, as shown in Fig. 3b. The lattice parameters of the coating samples gradually increased from 4.33 Å to 4.38 Å as rising Ti target power, indicating that the lattice of the TaN phase was distorted following the introduction of the Ti element, and that the lattice parameters of the (Ta, Ti)N phase are related to the Ti content [39]. Moreover, the full width at half maximum (FWHM) of the coating samples was calculated from the position of the (111) peak in the XRD patterns, as depicted in Fig. 3c. The analysis reveals that the FWHM of the doped samples is notably greater than that of the undoped ones, suggesting that the introduction of Ti elements reduces the grain size of the (Ta, Ti)N phase and enhances the compactness of the coatings.

3.3. Chemical state

To explore the chemical composition and bonding state of the (Ta, Ti)N layer, high-resolution XPS spectra of Ti 2p, Ta 4f, and N 1s were collected (Fig. 3d–f). All spectra were fitted using XPSpeak 4.1 software, with Lorentzian and Gaussian curves set to 20 % and 80 %, respectively. Three chemical bonds Ti-N, Ti-N-O, and O-Ti-O were identified in the Ti 2p spectrum (Fig. 3d), with the O element primarily derived from adsorption in the air [46]. The Ti 2p spectrum consists of Ti 2p3/2 and Ti 2p1/2 peaks, located within binding energy ranges of 453 eV–460 eV and 460 eV–470 eV, respectively. The Ti 2p3/2 peak at 454.5 eV and the Ti 2p1/2 peak at 461.5 eV confirm the presence of the Ti-N bond. In the Ta 4f spectrum (Fig. 3e), two chemical bonds Ta-N and Ta-O were detected. The Ta 4f spectrum is characterized by two peaks, Ta 4f7/2 and Ta 4f5/2, which are located at 23.6 eV and 25.5 eV, respectively, with a peak separation of 1.9 eV [47,48]. The introduction of Ti element results in a shift of the Ta 4f XPS peak towards higher binding energies. This is due to that the electronegativity of Ti (1.54) is slightly larger than that of Ta (1.5), and the addition of Ti attracts electrons around Ta, thereby reducing the shielding effect on the inner electrons [49]. In the N 1s spectrum (Fig. 3f), two chemical bonds N-O and N-metal were observed at 397.4 eV and 396 eV, respectively, and the presence of N-metal bonds confirms the formation of metal nitrides.

The internal area ratios of different bonds in the Ti 2p, Ta 4f, and N 1s spectra were calculated based on the fitted high-resolution XPS spectra. The proportion of Ti-N bonds increases from 15.6 % to 26.2 % with the Ti target power rises from 30 W to 150 W, demonstrating that higher Ti target power facilitates the formation of Ti-N bonds within the (Ta, Ti)N layer. Furthermore, when the Ti target power rises from 0 W to 150 W, the proportion of Ta-N bonds decreases from 38.2 % to 32.5 %, while the proportion of Ta-O bonds increases from 61.8 % to 67.5 %. This change can be attributed to the introducing of Ti element, which reduces the likelihood of reactions between N atoms and Ta atoms, resulting in more O atoms from the air reacting with tantalum to form Ta-O bonds. Additionally, N 1s spectrum analysis shows that with increasing Ti target power, the proportion of N-metal bonds in the (Ta, Ti)N layer rises from 18 % to 24 %, indicating that the growth rate of Ti-N bond formation is greater than the rate of decrease in Ta-N bonds.

3.4. Electrochemical tests

3.4.1. Potentiodynamic polarization results

Fig. 4a illustrates the potentiodynamic polarization curves of the samples, which are divided into three regions: cathode, anode, and passivation. The Tafel extrapolation method was employed to fit the polarization curves, and the corresponding electrochemical parameters are presented in Table 1. Since the corrosion potential of TiN is lower than that of TaN in the acidic environment of PEMFC, the corrosion potential (E_{corr}) of the coating samples decreases from −0.007 V to −0.175 V after Ti doping in the TaN layer. Nevertheless, the corrosion potentials of all coated samples remain higher than that of bare TC4 (−0.197 V), demonstrating the coatings' favorable chemical stability in the PEMFC acidic environment [50]. Notably, the corrosion current densities (I_{corr}) of the doped samples were 4.77×10^{-8} A/cm^2, 4.26×10^{-8} A/cm^2, 4.86×10^{-8} A/cm^2, 6.25×10^{-8} A/cm^2, and 8.74×10^{-8} A/cm^2, all of which were lower than that of the undoped sample (9.84×10^{-8} A/cm^2). This indicates that doping Ti into the TaN layer significantly improves the overall corrosion resistance of the coating [51]. Among them, the corrosion current density of the Ti/TiN/(Ta, Ti)N-60W sample is only 4.26×10^{-8} A/cm^2, significantly lower than the 2025 standard proposed by the DOE, and demonstrating excellent corrosion resistance and chemical stability. This phenomenon arises because, the morphology of the columnar crystal structure of the (Ta, Ti)N layer becomes indistinct, and the smallest grain size of the coating at a Ti target power of 60 W. This dense structure reduces the likelihood of corrosive media (H^+, SO_4^{2-}, and F^-) penetrating the matrix, thereby effectively protecting the TC4 substrate.

3.4.2. Potentiostatic polarization results

Since corrosion predominantly occurs on the cathode side of the PEMFC, the higher potential in this region tends to accelerate the corrosion rate of the coating by corrosive ions (H^+, SO_4^{2-}, and F^-) [5]. Hence, studying the long-term corrosion resistance of coated bipolar plates in the PEMFC cathode environment is essential. Fig. 4b presents the polarization curve of the samples at 0.6 V (vs. SCE) for 7200 s in a simulated PEMFC cathode environment. The corrosion current density of all coated samples dropped rapidly initially and then stabilized, indicating that the passive film on the coating surface was stable and resistant to damage in acidic conditions. In contrast, the slope of the curve for bare TC4 increased after a period of polarization, indicating that the initially formed passive film was insufficiently dense. As polarization time increases, the curve gradually levels off due to the reformation of the surface passive film. Fig. 4c illustrates the corrosion current density values ($I_{0.6V}$) for all samples. The $I_{0.6V}$ decreases steadily with increasing Ti target power, reaching a minimum of 8.98×10^{-8} A/cm^2 at 60 W. When Ti target power exceeds 60 W, the $I_{0.6V}$ gradually rises to 1.39×10^{-7} A/cm^2 but remains lower than the undoped sample's value of 3.84×10^{-7} A/cm^2.

The PEMFC generates a high potential (0.9–1.1 V (vs. SCE)) during the vehicle's start and shutdown processes, which accelerates the degradation of the bipolar plate [52,53]. However, during the process, a transient cathode high potential duration of approximately 10 ms was observed on the bipolar plate surface. According to road operation data, fuel cell vehicles can start and stop up to 38,500 times within 5000 h of operation, with a cumulative duration of only 385 s. Therefore, this study investigated the long-term durability of the coating sample by polarizing at 1.2 V (vs. SCE) for 3600 s, which fully met the test standards. Fig. 4d illustrates the potentiostatic polarization curve of the coating samples at 1.2 V (vs. SCE). Notably, the Ti/TiN/(Ta, Ti)N-60W sample exhibits the fastest passivation response, indicating that this coating is the most stable in a cathodic environment at 1.2 V (vs. SCE). However, the slope of the corrosion current density curve for the undoped sample increases slightly during the later stages of polarization, indicating that the undoped sample exhibits poor stability at a potential of 1.2 V (vs. SCE). Additionally, several samples exhibited numerous spikes in their corrosion current density curves during polarization, which represent unstable fluctuations resulting from inhomogeneous corrosion due to pores and pinholes within the coating. Fig. 4e shows the corrosion current density value ($I_{1.2V}$) of the coating samples after the curve stabilizes. As the Ti target power increases, the $I_{1.2V}$ of the coating samples initially decreases from 2.54×10^{-6} A/cm^2 (0 W) to 0.941×10^{-6} A/cm^2 (60 W) before subsequently increasing to 1.61×10^{-6} A/cm^2 (150 W). It is worth noting that the corrosion current density of the Ti/TiN/(Ta, Ti)N-60W sample was the lowest (0.941×10^{-6} A/cm^2), indicating that this sample possesses superior resistance to high potential corrosion at 1.2 V (vs. SCE), while other samples remain susceptible to failure.

Fig. 4f–k illustrates the surface micro-morphology of the samples after potentiostatic polarization at 1.2 V (vs. SCE) for 3600 s. A significant number of localized corrosion dark zones were observed on the surface of the undoped sample, where the coating suffered severe damage (Fig. 4f). This is attributed to the highly developed columnar crystal structure of the TaN layer (Fig. 2g), which provides a large number of channels for the invasion of corrosive media, resulting in severe localized corrosion. As the Ti target power increases, these corrosion dark zones decrease significantly, and the corrosion traces on the surface of the coating become less pronounced at a Ti target power of 60 W (Fig. 4h). This phenomenon can be attributed to the relatively dense coating structure at a Ti target power of 60 W, which effectively minimizes the immersion of corrosive media, thereby providing adequate protection for the substrate. However, at Ti target powers of 120 W and 150 W, noticeable pitting defects appear on the sample's

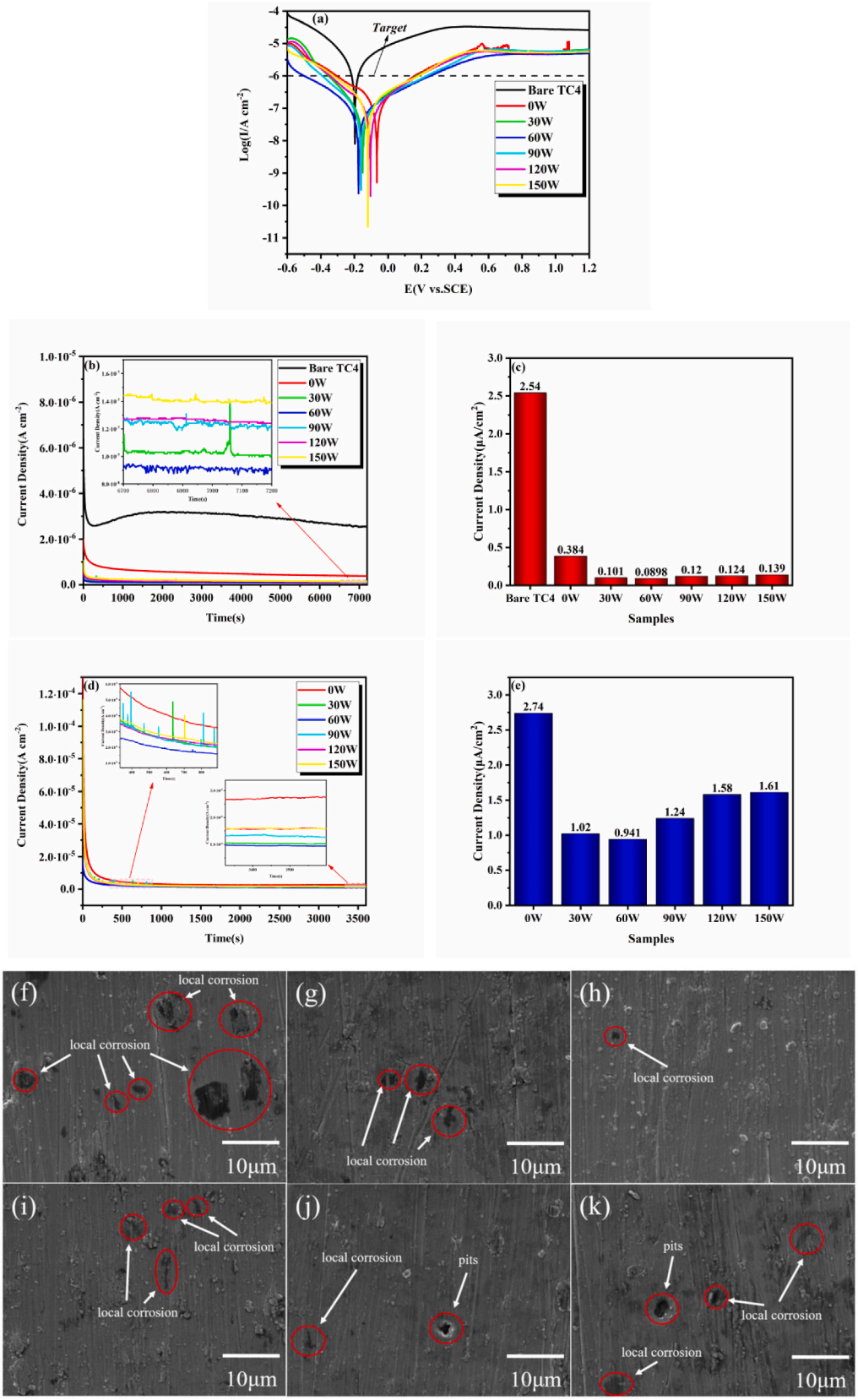

Fig. 4. (a) potentiodynamic polarization curves. (b) potentiostatic polarization curves (0.6 V vs. SCE). (c) Stabilized corrosion current density (0.6 V vs. SCE) (d) potentiostatic polarization curves (1.2 V vs. SCE). (e) Stabilized corrosion current density (1.2 V vs. SCE). SEM surface morphology of the sample after potentiostatic polarization at 1.2 V (vs. SCE): (f) 0 W. (g) 30 W. (h) 60 W. (i) 90 W. (j) 120 W. (k) 150 W.

Table 1
Electrochemical parameters of samples.

Samples	E_{corr}/V (vs. SCE)	I_{corr}/ A·cm^{-2}	β_a/ V·dec^{-1}	β_c/ V·dec^{-1}
Bare TC4	−0.197	3.68 × 10^{-6}	0.488	0.257
Ti/TiN/(Ta,Ti)N-0W	−0.07	9.84 × 10^{-8}	0.166	0.1
Ti/TiN/(Ta,Ti)N-30W	−0.151	4.77 × 10^{-8}	0.132	0.168
Ti/TiN/(Ta,Ti)N-60W	−0.175	4.26 × 10^{-8}	0.157	0.182
Ti/TiN/(Ta,Ti)N-90W	−0.16	4.86 × 10^{-8}	0.15	0.180
Ti/TiN/(Ta,Ti)N-120W	−0.105	6.25 × 10^{-8}	0.158	0.164
Ti/TiN/(Ta,Ti)N-150W	−0.12	8.74 × 10^{-8}	0.157	0.184

surface, significantly larger than those observed prior to corrosion (Fig. 4j and k). This may be attributed to the accumulation of corrosive media within these pits, exacerbating the degree of erosion. Furthermore, higher Ti target powers can induce nano-galvanic corrosion within the (Ta, Ti)N layer, which accelerates both the corrosion and detachment of the coating, resulting in larger pitting defects. The primary cause of this nano-galvanic corrosion is the differing electrochemical activities of TiN and TaN within the (Ta, Ti)N layer. Under standard electrode potential conditions, TiN has a relatively negative potential, while TaN has a relatively positive potential, creating a potential difference between the two phases. When the coating contains both TiN and TaN phases, nano-scale galvanic couples can form at their interface, leading to severe local corrosion upon the invasion of corrosive media [54,55]. Additionally, higher Ti target power promotes the localized enrichment of TiN phase within the (Ta, Ti)N layer, further increasing the potential difference between TiN and TaN. At the same time, it leads to the formation of a Ti matel phase in the coating that does not undergo nitridation, which matel phase also forms a galvanic couple with TiN and TaN, thereby aggravating the degree of galvanic corrosion.

3.4.3. EIS tests

To further investigate the corrosion behavior of the samples in the PEMFC environment, electrochemical impedance spectroscopy (EIS) was employed for analysis. The Nyquist plot (Fig. 5a) reveals that all samples exhibit two distinct capacitive semicircles. Among them, the size of the capacitive semicircle in the low-frequency region correlates with the charge transfer resistance value. A larger semicircle diameter indicates a lower corrosion rate of the coating. Compared with the

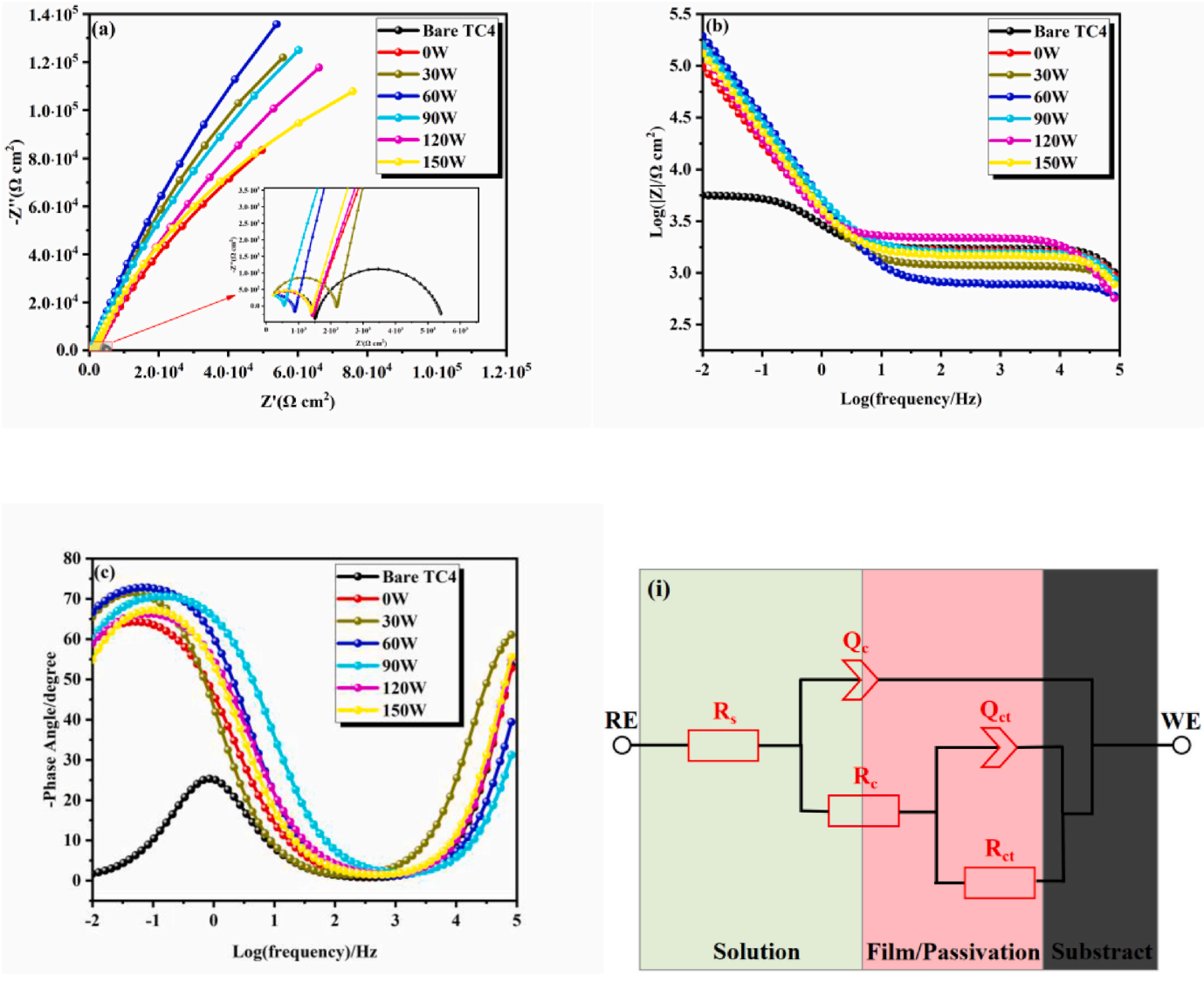

Fig. 5. (a) nyquist plot. bode plot for (b) frequency-|Z| and (c) frequency-phase angle. (d) equivalent circuits.

undoped sample, the capacitive semicircle diameter of the Ti-doped sample is significantly larger in the low-frequency region, indicating that doping Ti in the TaN layer markedly enhances the corrosion resistance of the coating [56]. In general, the low-frequency, mid-frequency, and high-frequency regions of the Bode diagram correspond to the contact characteristics between the coating and the substrate, the corrosion behavior within the coating, and the contact characteristics between the coating and the corrosive medium, respectively [57]. The frequency-phase angle diagram (Fig. 5c) shows that the Ti-doped sample exhibits a broader frequency range in the mid-frequency and low-frequency regions, with a significantly higher maximum phase angle compared to the undoped sample, which indicating that doping Ti in the TaN layer enhances the chemical stability of the coating [58]. Furthermore, as the Ti target power increases, the phase angle in the low-frequency region initially rises and then declines, indicating that the tendency for local microporous corrosion of the coating decreases first and then increases with increasing Ti target power. Notably, the Ti/TiN/(Ta, Ti)N-60W sample exhibits the largest |Z| value and phase angle in the low-frequency region, as well as the widest peak in both the low- and mid-frequency regions (Fig. 5b–c), indicating that the Ti/TiN/(Ta, Ti)N-60W sample possesses excellent passivation properties and corrosion resistance.

To provide a more intuitive assessment of the coating's corrosion resistance, the EIS data for all samples were fitted using Zview 3.3 software. The Nyquist and Bode plots reveal that all samples exhibit two independent time constants in the frequency domain, indicating that they share similar corrosion behavior. Consequently, an equivalent circuit model with dual time constants was employed to simulate the impedance characteristics of bare TC4 and coated samples (Fig. 5d). R_{ct}, R_c, and R_s represent the charge transfer resistance, the resistance of corrosion products, and the solution resistance between the coating and the SCE, respectively, while Q_{ct} and Q_c denote the double-layer capacitance and the capacitance of corrosion products, respectively [59,60]. Table 2 presents the electrochemical parameters derived from fitting the data by Zview 3.3 software. The R_{ct} value is significantly greater than the R_c value, indicating that the impedance of the coating is primarily influenced by the R_{ct} value. The R_{ct} value is associated with the diffusion resistance of corrosive ions and indicates the ability to prevent the dissolution of metal ions. The table indicates that the R_{ct} value of the doped coating is significantly higher than that of the undoped coating. Notably, the TiN/(Ta, Ti)N-60W sample exhibits the highest R_{ct} value of 1.04×10^6 Ω cm^2, indicating that the coating provides the greatest resistance to corrosive ion transfer and offers superior protection to the substrate, aligning with the findings from previous analyses. Additionally, the R_{ct} value is typically related to the porosity of the coating. A larger R_{ct} value indicates higher coating integrity and lower porosity, while a smaller R_{ct} value suggests a coating with more pores or defects. Therefore, the porosity (P) of the coating can be indirectly determined from the R_{ct} value obtained by fitting the EIS data [61]:

$$P = 100\% \times \left(\frac{R_{cts}}{R_{ctc}}\right) \quad (6)$$

Among them, R_{cts} and R_{ctc} represent the charge transfer resistance values of bare TC4 and coating samples, respectively. Table 2 shows that as the Ti target power increases, the porosity of the doped sample decreases from 0.50 % to 0.38 % before subsequently increasing to 0.77 %, remaining consistently lower than that of the undoped sample (0.99 %). The reduction in the porosity of the coating indicates that doping the Ti element into the TaN layer enhances the coating's compactness, thereby improving its corrosion resistance.

3.5. ICR and hydrophobicity tests

The bipolar plate in the PEMFC serves to collect and conduct current, a higher ICR increases power loss and reduces electron transfer efficiency, which negatively impacts the output efficiency of the PEMFC [62,63]. Fig. 6a depicts the relationship curve between the ICR value and the compaction force for the fresh sample. At the initial stage of pressurization, all samples exhibit a rapid decrease in ICR, attributed to an increased effective contact area between the specimen and the carbon paper, which facilitates greater electron conduction. As compaction force continues to increase, the ICR curves of all specimens decrease more gradually as near-complete contact is achieved between the specimens and the carbon paper. Fig. 6b illustrates the ICR values of all samples before and after polarization, measured at the standard assembly pressure of the PEMFC (140 N/cm^2). Initially, the ICR value of bare TC4 is the highest, reaching 98.25 mΩ cm^2, which is attributed to the spontaneous formation of a passivation film on its surface. Additionally, the ICR values of the doped samples are significantly lower than those of the undoped sample. As Ti target power increases, the ICR value of the coated samples decreases from 6.85 mΩ cm^2 to 4.22 mΩ cm^2. The enhancement in the conductivity of the coating following Ti doping can be attributed to two key factors. Firstly, Ti doping reduces the grain size of the coating, providing more electron transmission pathways and thus enhancing conductivity. Secondly, Ti doping increases the proportion of the TiN phase (with a conductivity of 4.55×10^6 S/m) while decreasing the proportion of the TaN phase (with a conductivity of 10^5–10^6 S/m), resulting in improved overall conductivity [64].

Notably, at 0.6 V (vs. SCE), the ICR value of the coating samples gradually decreased from 9.68 mΩ cm^2 to 6.87 mΩ cm^2 as the Ti target power increased. The ICR values showed no significant change after polarization, confirming that the coating maintained high conductivity at this potential. However, at 1.2 V (vs. SCE), as Ti target power increases, the ICR value of the coating decreased from 54.26 mΩ cm^2 (0 W) to 42.58 mΩ cm^2 (60 W), and then rising again to 52.38 mΩ cm^2 (150 W). As Ti target power increases from 0 W to 60 W, the coating structure becomes denser, reducing corrosion and thus decreasing the ICR value. When the Ti target power exceeds 60 W, the reduction in the conductivity of the coating is primarily attributed to the increased TiN content in the (Ta, Ti)N layer, which leads to a higher formation of TiN_xO_y due to oxidation [49].

Water generated during the operation of the PEMFC accumulates in the flow channel of the bipolar plate. If not promptly removed, this water adheres to the bipolar plate, exacerbating its deterioration, thus studying the hydrophobicity of the coating is essential [65,66]. The hydrophobicity of a coating is typically characterized by the water contact angle, and Fig. 7 illustrates the water contact angles of all samples. It is worth noting that the bare TC4 exhibits the smallest water contact angle (66.6°), indicating poor hydrophobicity, which attributed to the significant presence of polar Ti-O bonds on its surface [67].

Table 2
Equivalent circuit fitting parameters of the sample.

Sample	R_s (Ω·cm^2)	R_c (Ω·cm^2)	Q_c (F·cm^2)	N_c	R_{ct} (Ω·cm^2)	Q_{ct} (F·cm^2)	N_{ct}	P
Bare TC4	5.61	1.71×10^3	1.55×10^{-9}	0.925	3.95×10^3	1.13×10^{-4}	0.891	/
Ti/TiN/(Ta,Ti)N-0W	5.34	1.6×10^3	2.29×10^{-9}	0.977	4.01×10^5	8.24×10^{-5}	0.941	0.99 %
Ti/TiN/(Ta,Ti)N-30W	5.56	2.1×10^3	8.99×10^{-9}	0.977	7.96×10^5	7.71×10^{-5}	0.975	0.50 %
Ti/TiN/(Ta,Ti)N-60W	5.27	1.17×10^3	3.6×10^{-9}	0.934	1.04×10^6	5.69×10^{-5}	0.982	0.38 %
Ti/TiN/(Ta,Ti)N-90W	5.15	1.08×10^3	5.99×10^{-9}	0.904	7.31×10^5	4.48×10^{-5}	0.964	0.54 %
Ti/TiN/(Ta,Ti)N-120W	5.46	1.54×10^3	1.82×10^{-9}	1	6.46×10^5	5.11×10^{-5}	0.952	0.61 %
Ti/TiN/(Ta,Ti)N-150W	5.18	1.47×10^3	3.19×10^{-9}	0.96	5.13×10^5	6.31×10^{-5}	0.944	0.77 %

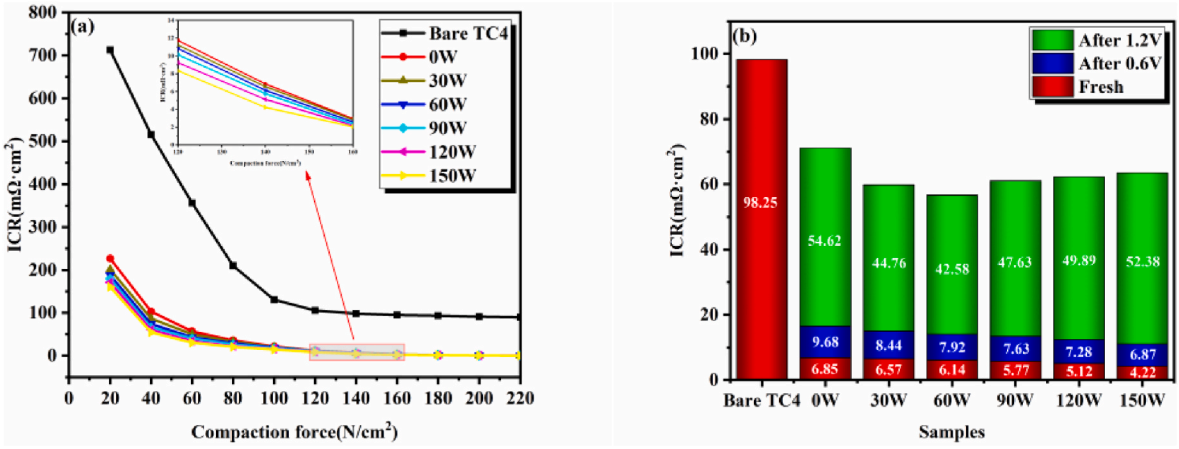

Fig. 6. (a) ICR values of bare TC4 and coated samples at various Ti target powers. (b) ICR values of the coating samples before and after corrosion at a compaction force of 140 N/cm^2.

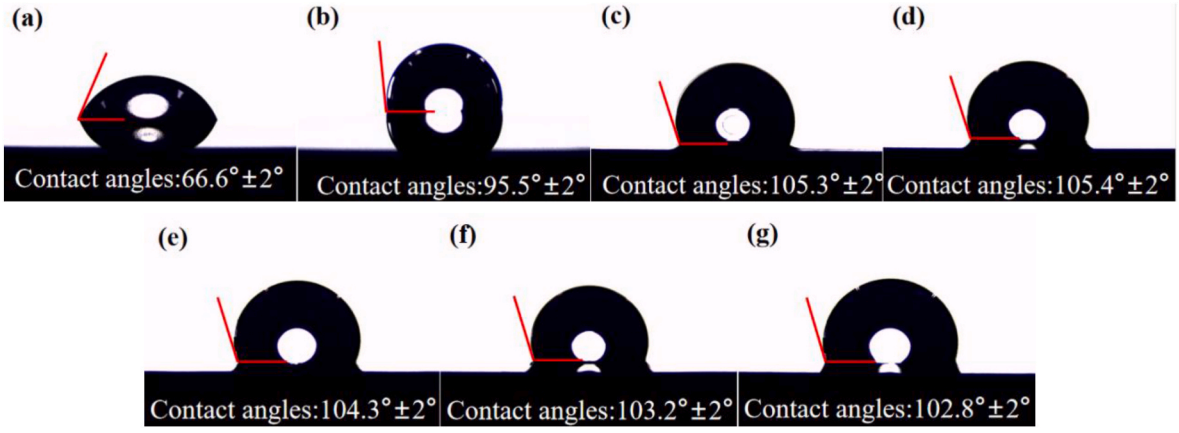

Fig. 7. Water contact angle of the samples: (a) Bare TC4. (b) 0 W. (c) 30 W. (d) 60 W. (e) 90 W. (f) 120 W. (g) 150 W.

Compared to the undoped samples, the water contact angles of the doped samples exceed 100°. Notably, the Ti/TiN/(Ta, Ti)N-60W sample exhibits the highest water contact angle of 105.4°, demonstrating excellent hydrophobic properties. The enhanced hydrophobicity of the coating results from the interplay between its surface composition and structure. Doping the Ti element refines the grain size of the coating, thereby enhancing its compactness. Moreover, the introduction of the Ti element increases the proportion of N-metal bonds in the (Ta, Ti)N layer, reducing the surface energy of the coating, minimizing its contact area with the corrosive electrolyte, and ultimately enhancing the service life of the bipolar plate.

3.6. Anti-corrosion mechanism

At 0.6 V (vs. SCE), both TaN and TiN exhibit strong corrosion resistance, meaning that the coating's overall resistance to corrosion at this potential is primarily determined by its microstructure [31,32]. In the previous 0.6 V (vs. SCE) potentiostatic tests, the corrosion current density decreased from 3.84 × 10^{-7} A/cm^2 (0 W) to 8.98 × 10^{-8} A/cm^2 (60 W), but then increased to 1.39 × 10^{-7} A/cm^2 (150 W) as the Ti target power rise. The columnar crystal structure of the (Ta, Ti)N layer becomes more compact, and the grain size decreases as the Ti target power increases from 0 W to 60 W. This denser structure effectively blocks the penetration of corrosive media into the intermediate layer and substrate, offering enhanced protection for the TC4 substrate. As for the coating structure becomes porous and the risk of galvanic corrosion increases when the Ti target power exceeds 60 W, leading to a slight increase in corrosion current density, but due to the excellent chemical stability of TaN and TiN under 0.6 V (vs. SCE) potential, ensure the corrosion current density remains below the 2025 DOE performance standard.

Due to the lower chemical stability of TiN compared to TaN at the high potential of 1.2 V (vs. SCE), TiN is more susceptible to oxidation and dissolution in the PEMFC environment [49]. As a result, the corrosion resistance of the coating is primarily influenced by its chemical composition and microstructure. In the previous 1.2 V (vs. SCE) potentiostatic test, as Ti target power increased, the corrosion current density of the coating decreased from 2.54 × 10^{-6} A/cm^2 (0 W) to 9.41 × 10^{-7} A/cm^2 (60 W), and then increased to 1.61 × 10^{-6} A/cm^2 (150 W). Without doping, the TaN layer has a loose structure, allowing corrosive medium easily penetrate and react with the TiN layer, forming TiN_xO_y (Equ. 7) [49]. However, TiN_xO_y dissolves in the presence of F^- and H^+ ions from the corrosive medium in an acidic environment (Equ. 8) [68], eventually leading to coating failure (Fig. 8a). With a small amount of Ti doping (60 W), due to in direct contact with the corrosive medium, the TiN phase on the surface undergoes oxidation and dissolution. However, its content in the (Ta, Ti)N layer is low, and the denser structure of the (Ta, Ti)N layer slows down the corrosion process (Fig. 8b). However, excessive Ti doping (150 W) results in a loose structure of the (Ta, Ti)N layer, accompanied by an increase in the TiN content. On one hand, the increase in TiN content intensifies the oxidative dissolution of the TiN phase. On the other hand, the TiN phase, acting as the anode, undergoes severe nano-galvanic corrosion at high potential, accelerating its oxidative dissolution and resulting in an

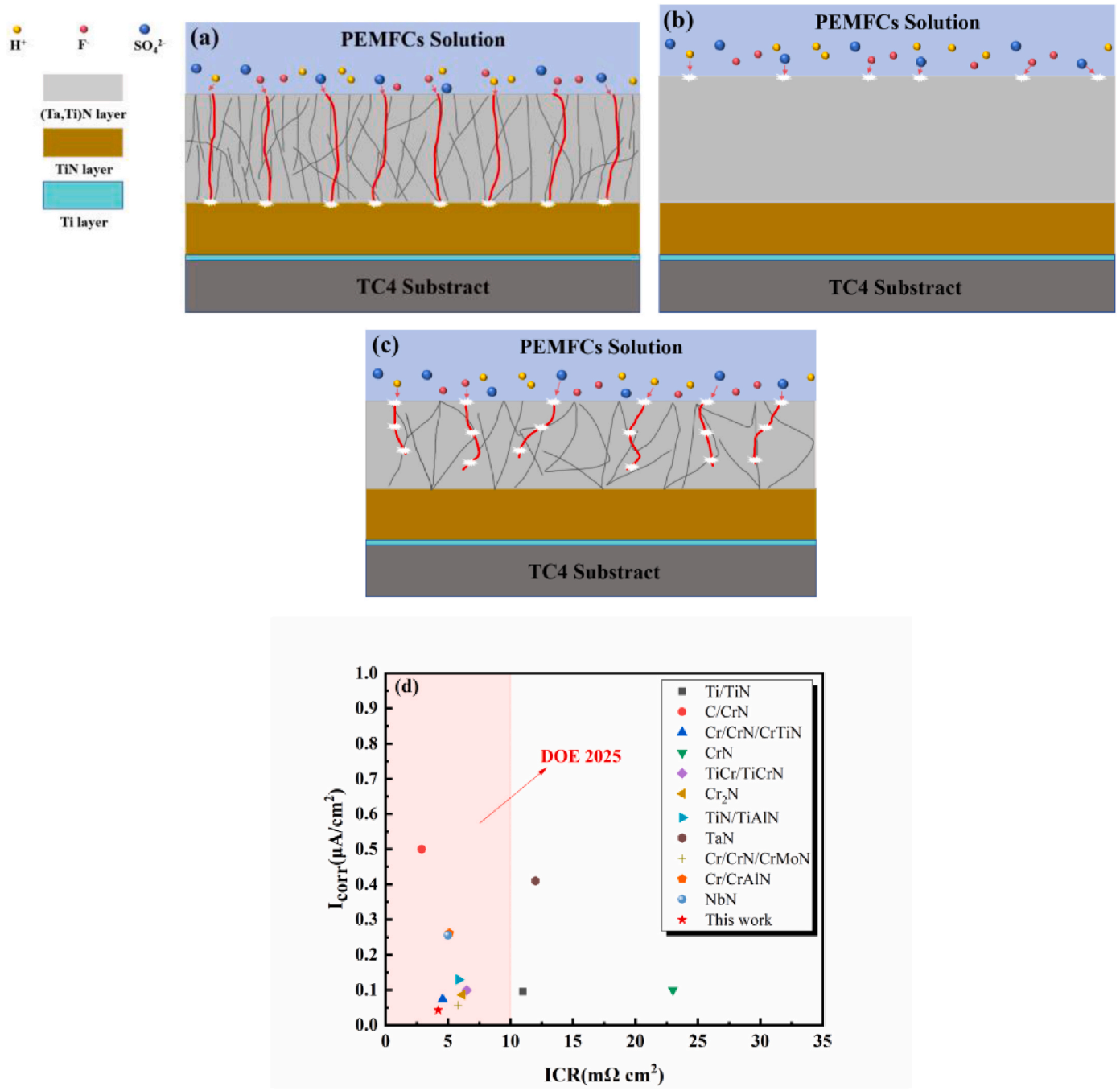

Fig. 8. Corrosion mechanism of coating: (a) Undoped sample. (b) 60 W doped sample. (c) 150 W doped sample. (c) Comprehensive comparison of I_{corr} and ICR values of metal nitride coatings reported in this work and in recent years [7,27,34,69–76].

increase in corrosion current density (Fig. 8c).

$$TiN + ((y-1)/2)O_2 + H_2O = TiN_xO_y + ((1-x)/2)N_2 + H_2 \quad (7)$$

$$TiN_xO_y + 6F^- + (4x+2y)H^+ = [TiF_6]^{2-} + xNH^{4+} + yH_2O \quad (8)$$

In this work, Ti doping in the Ti/TiN/(Ta, Ti)N coating enhanced its density and facilitated the formation of a highly conductive TiN phase, thereby significantly improving its corrosion resistance and electrical conductivity. Compared to most metal nitride coatings, this coating demonstrates superior performance and holds significant potential for application as a protective layer for metal bipolar plates (Fig. 8d).

4. Conclusion

This study examines the effect of Ti target power on the microstructure, corrosion resistance, conductivity, and hydrophobicity of Ti/TiN/(Ta, Ti)N coatings. The primary conclusions are as follows:

(1) The (Ta, Ti)N phase was formed following the doping of Ti into the TaN layer, with the proportion of nitride content in the coating gradually increasing as the Ti target power rises. Lower of Ti target power (<60 W) inhibits the formation of the columnar crystal structure of the coating, reduces the grain size, and increases its thickness. However, higher of Ti target power (>120

W) promotes the development of the columnar crystal structure and decreasing the coating's thickness.

(2) The Ti/TiN/(Ta, Ti)N-60W sample exhibits a low corrosion current density of 4.26×10^{-8} A/cm^2, with corrosion current densities of only 8.98×10^{-8} A/cm^2 and 9.41×10^{-7} A/cm^2 observed in the potentiostatic polarization tests at 0.6 V (vs. SCE) and 1.2 V (vs. SCE), respectively.

(3) The ICR value of the coating decreases from 6.85 mΩ cm^2 to 4.22 mΩ cm^2 as the Ti target power increases a a compaction force of 140 N/cm^2, thereby meeting the 2025 DOE standard. Furthermore, the Ti/TiN/(Ta, Ti)N-60W sample demonstrates the largest water contact angle of 105.4°, indicating excellent hydrophobicity.

CRediT authorship contribution statement

Wei Li: Writing – review & editing, Investigation, Funding acquisition. **Yong Wang:** Writing – review & editing, Writing – original draft, Software, Investigation, Formal analysis, Data curation. **Xiulan Li:** Formal analysis, Data curation. **Xinjun Zhou:** Formal analysis, Data curation, Conceptualization. **Xiao Jiang:** Software, Data curation. **Can Xiong:** Software, Data curation. **Yao Chen:** Software, Data curation. **Fei You:** Software, Data curation. **Zhengyu Guo:** Software, Data curation. **Yuan Zhang:** Software, Data curation. **Lintao Liu:** Software, Investigation. **Xuan Li:** Software, Data curation.

Declaration of competing interest

The authors declare that they have no known competing financial interests or personal relationships that could have appeared to influence the work reported in this paper.

Acknowledgment

This research was financially supported by the Key Research and Development Project of Sichuan Province Science and Technology Department (No. 2023YFG0239), the Scientific Research and Innovation Team Program of Sichuan University of Science and Engineering (No. H92322), and the Graduate Innovation Fund Project of Sichuan University of Science & Engineering (No. Y2023080, Y2024015, Y2024024, and Y2024012).

Data availability

Data will be made available on request.

References

[1] H. Ren, X. Meng, Y. Lin, Z. Shao, Independent regulation of ionomer distribution in catalyst layer for proton exchange membrane fuel cell, Electrochim. Acta 462 (2023) 142710, https://doi.org/10.1016/j.electacta.2023.142710.

[2] B.S. Mi, Q. Wang, T.W. Qi, Z.W. Qin, Z. Chen, H.B. Wang, Performance and structure of Ti-doped amorphous carbon/CrN/Ti multilayer coating deposited on 316L stainless steel for use as bipolar plate in proton exchange membrane fuel cell, J. Alloys Compd. 943 (2023) 169080, https://doi.org/10.1016/j.jallcom.2023.169080.

[3] I. Khalakhan, L. Supik, M. Vorokhta, Compositionally tuned magnetron cosputtered PtxNi100-x alloy as a cathode catalyst for proton exchange membrane fuel cells, Appl. Surf. Sci. 511 (2020) 145486, https://doi.org/10.1016/j.apsusc.2020.145486.

[4] L. Wang, Y. Tao, Z. Zhang, Y. Wang, Q. Feng, H. Wang, H. Li, Molybdenum carbide coated 316L stainless steel for bipolar plates of proton exchange membrane fuel cells, Int. J. Hydrogen Energy 44 (10) (2019) 4940–4950, https://doi.org/10.1016/j.ijhydene.2018.12.184.

[5] J. Jin, J. Zhang, M. Hu, X. Li, Investigation of high potential corrosion protection with titanium carbonitride coating on 316l stainless steel bipolar plates, Corrosion Sci 191 (2021) 109757, https://doi.org/10.1016/j.corsci.2021.109757.

[6] F. Tian, X. Tao, J. Wang, Z. Huang, W. Tian, J. Chen, Investigation of Cu-doped amorphous carbon film in improving corrosion resistance and interfacial conductivity of proton exchange membrane fuel cell, Surf. Coating. Technol. 485 (2024) 130926, https://doi.org/10.1016/j.surfcoat.2024.130926.

[7] J.Y. Chen, S. Zhang, J. Zheng, Y.F. Dong, C.X. Zhang, J.C. Li, Z.L. Chen, J. Zhang, D. Sun, Excellent anti-corrosion and conductivity of NbN coated on Ti bipolar plate by controlling N_2 flow rates, J. Alloys Compd. 976 (2024) 173033, https://doi.org/10.1016/j.jallcom.2023.173033.

[8] H. Choi, H. Eun Kang, D.J. Kim, Y. Soo Yoon, A comprehensive review of stainless-steel bipolar plate coatings and their role in mitigating corrosion in aggressive proton-exchange membrane fuel cells environments, Chem. Eng. J. 493 (2024) 152662, https://doi.org/10.1016/j.cej.2024.152662.

[9] V.E. Pukha, A.A. Glukhov, A.A. Belmesov, E.N. Kabachkov, I.I. Khodos, M. Khadem, P.A. Karaseov, Corrosion-resistant nanostructured carbon-based coatings for applications in fuel cells based on bipolar plates, Vacuum 218 (2023) 112643, https://doi.org/10.1016/j.vacuum.2023.112643.

[10] A.V. Ingle, V.S. Raja, J. Rangarajan, P. Mishra, Corrosion resistant Al-Cr-Mo alloy coating on type 316L stainless steel bipolar plates for proton exchange membrane fuel cell applications, Fuel Cell. 19 (6) (2019) 708–723, https://doi.org/10.1002/fuce.201900122.

[11] O.A. Alo, I.O. Otunniyi, H.C.Z. Pienaar, Development of graphite-filled polymer blends for application in bipolar plates, Polym. Compos. 41 (8) (2020) 3364, https://doi.org/10.1002/pc.25625, 337.

[12] Q. Hu, J.Y. Gao, S. Shu, Y.X. Xu, J.L. Luo, X.Z. Wang, Corrosion behaviors of multilayer C/Cr/SS bipolar plates for proton exchange membrane fuel cells under dynamic potential polarization based on New European Driving Cycle, Corrosion Sci. 214 (2023) 111032, https://doi.org/10.1016/j.corsci.2023.111032.

[13] Y. Yang, X. Ning, H. Tang, L. Guo, H. Liu, Effects of passive films on corrosion resistance of uncoated SS316L bipolar plates for proton exchange membrane fuel cell application, Appl. Surf. Sci. 320 (2014) 274–280, https://doi.org/10.1016/j.apsusc.2014.09.049.

[14] S. Peng, J. Xu, Z.H. Xie, Titanium bipolar plates augmented by nanocrystalline TiZrHfMoW coatings for application in proton exchange membrane fuel cells, Appl. Surf. Sci. 591 (2022) 153200, https://doi.org/10.1016/j.apsusc.2022.153200.

[15] T. Wilberforce, Z.E. Hassan, E. Ogungbemi, O. Ijaodola, F.N. Khatib, A comprehensive study of the effect of bipolar plate (BP) geometry design on the performance of proton exchange membrane (PEM) fuel cells, Renew. Sustain. Energy Rev. 111 (2019) 236–260, https://doi.org/10.1016/j.rser.2019.04.081.

[16] Q. Feng, X. Yuan, G. Liu, B. Wei, Z. Zhang, H. Li, H. Wang, A review of proton exchange membrane water electrolysis on degradation mechanisms and mitigation strategies, J. Power Sources 366 (2017) 33–55, https://doi.org/10.1016/j.jpowsour.2017.09.006.

[17] T.J. Toops, M.P. Brady, F.Y. Zhang, H.M. Meyer, K. Ayers, A. Roemer, L. Dalton, Evaluation of nitrided titanium separator plates for proton exchange membrane electrolyzer cells, J. Power Sources 272 (2014) 954–960, https://doi.org/10.1016/j.jpowsour.2014.09.016.

[18] M.F. Khan, A.Y. Adesina, Z.M. Gasem, Electrochemical and electrical resistance behavior of cathodic arc PVD TiN, CrN, AlCrN, and AlTiN coatings in simulated proton exchange membrane fuel cell environment, Mater. Corros. 70 (2019) 281–292, https://doi.org/10.1002/maco.201810377.

[19] H.Y. Jung, S.Y. Huang, B.N. Popov, High-durability titanium bipolar plate modified by electrochemical deposition of platinum for unitized regenerative fuel cell (URFC), J. Power Sources 195 (7) (2010) 1950, https://doi.org/10.1016/j.jpowsour.2009.10.002.

[20] J. Kai, X.Y. Lin, L.H. Li, H.S. Tian, Active screen plasma surface co-alloying treatments of 316 stainless steel with nitrogen and silver for fuel cell bipolar plates, Surf. Coating. Technol. 283 (2015) 122–128, https://doi.org/10.1016/j.surfcoat.2015.10.038.

[21] Y. Wang, S. Zhang, Z. Lu, L. Wang, W. Li, Preparation and performances of electrically conductive Nb-doped TiO2 coatings for 316 stainless steel bipolar plates of proton-exchange membrane fuel cells, Corrosion Sci 142 (2018) 249–257, https://doi.org/10.1016/j.corsci.2018.07.034.

[22] D. Zhang, P. Yi, L. Peng, X. Lai, J. Pu, Amorphous carbon films doped with silver and chromium to achieve ultra-low interfacial electrical resistance and long-term durability in the application of proton exchange membrane fuel cells, Carbon 145 (2019) 333–344, https://doi.org/10.1016/j.carbon.2019.01.050.

[23] K. Hou, P. Yi, L. Peng, X. Lai, Niobium doped amorphous carbon film on metallic bipolar plates for PEMFCs: first principle calculation, microstructure and performance, Int. J. Hydrogen Energy 44 (2019) 3144–3156, https://doi.org/10.1016/j.ijhydene.2018.12.040.

[24] H.Q. Fan, D.D. Shi, X.Z. Wang, J.L. Luo, J.Y. Zhang, Q. Li, Enhancing through-plane electrical conductivity by introducing Au microdots onto TiN coated metal bipolar plates of PEMFCs, Int. J. Hydrogen Energy 45 (2020) 29442–29448, https://doi.org/10.1016/j.ijhydene.2020.07.270.

[25] A.P. Nowak, T.T. Salguero, K.W. Kirby, F. Zhong, R.H.J. Blunk, A conductive and hydrophilic bipolar plate coating for enhanced proton exchange membrane fuel cell performance and water management, J. Power Sources 210 (2012) 138–145, https://doi.org/10.1016/j.jpowsour.2012.03.005.

[26] V. Bonu, M. Jeevitha, V. Praveen Kumar, S. Bysakh, H.C. Barshilia, Ultra-thin multilayered erosion resistant Ti/TiN coatings with stress absorbing layers, Appl. Surf. Sci. 478 (2019) 872–881, https://doi.org/10.1016/j.apsusc.2019.02.012.

[27] J. Jin, H. Liu, D. Zheng, Z. Zhu, Effects of Mo content on the interfacial contact resistance and corrosion properties of CrN coatings on SS316L as bipolar plates in simulated PEMFCs environment, Int. J. Hydrogen Energy 43 (2018) 10048–10060, https://doi.org/10.1016/j.ijhydene.2018.04.044.

[28] D. Zhang, L. Duan, L. Guo, Z. Wang, J. Zhao, W.H. Tuan, K. Niihara, TiN-coated titanium as the bipolar plate for PEMFC by multi-arc ion plating, Int. J. Hydrogen Energy 36 (2011) 9155–9161, https://doi.org/10.1016/j.ijhydene.2011.04.123.

[29] P. Yi, C. Dong, T. Zhang, K. Xiao, Y. Ji, J. Wu, X. Li, Effect of plasma electrolytic nitriding on the corrosion behavior and interfacial contact resistance of titanium in

the cathode environment of proton-exchange membrane fuel cells, J. Power Sources 418 (2019) 42–49, https://doi.org/10.1016/j.jpowsour.2019.02.043.
[30] T. Li, Z. Yan, Z. Liu, Y. Yan, Y. Chen, Surface microstructure and performance of TiN monolayer film on titanium bipolar plate for PEMFC, Int. J. Hydrogen Energy 46 (2021) 31382–31390, https://doi.org/10.1016/j.ijhydene.2021.07.021.
[31] Z. Yan, T. Li, Q. Wang, H. Li, Y. Wang, C. Wu, Y. Yan, Y. Chen, Surface conductivity and preferred orientation of TiN film for Ti bipolar plate, Coatings 12 (2022) 454, https://doi.org/10.3390/coatings12040454.
[32] C. Choe, H. Choi, W. Hong, J.J. Lee, Tantalum nitride coated AISI 316L as bipolar plate for polymer electrolyte membrane fuel cell, Int. J. Hydrogen Energy 37 (2012) 405–411, https://doi.org/10.1016/j.ijhydene.2011.09.060.
[33] J. Jin, Z. He, X. Zhao, Effect of Al content on the corrosion resistance and conductivity of metal nitride coating in the cathode environment of PEMFCs, Mater. Chem. Phys. 245 (2020) 122739, https://doi.org/10.1016/j.matchemphys.2020.122739.
[34] F. Bi, P. Yi, T. Zhou, L. Peng, X. Lai, Effects of Al incorporation on the interfacial conductivity and corrosion resistance of CrN film on SS316L as bipolar plates for proton exchange membrane fuel cells, Int. J. Hydrogen Energy 40 (2015) 9790–9802, https://doi.org/10.1016/j.ijhydene.2015.06.012.
[35] F.Y. Yan, B.L. Jiang, Z.Y. Wang, J. Shi, Effect of thermal activation energy on the structure and conductivity corrosion resistance of Cr doped TiN films on metal bipolar plate, Mater. Chem. Phys. 287 (2022) 126082, https://doi.org/10.1016/j.matchemphys.2022.126082.
[36] S. Peng, J. Xu, Z.Y. Li, S.Y. Jiang, P. Munroe, A reactive-sputter-deposited TiSiN nanocomposite coating for the protection of metallic bipolar plates in proton exchange membrane fuel cells, Ceram. Int. 46 (3) (2020) 2743–2757, https://doi.org/10.1016/j.ceramint.2019.09.263.
[37] S.P. Mani, P. Agilan, M. Kalaiarasan, Effect of multilayer CrN/CrAlN coating on the corrosion and contact resistance behavior of 316L SS bipolar plate for high temperature proton exchange membrane fuel cell, J. Mater. Sci. Technol. 97 (2022) 134–146, https://doi.org/10.1016/j.jmst.2021.04.043.
[38] Z.J. Wu, R.L. Liu, Z.H. Liu, X.Y. Wu, F.L. Li, Microstructure and property of multilayer TiN/TiCN nanocrystalline coating used for metal bipolar plate, Vacuum 227 (2024) 113361, https://doi.org/10.1016/j.vacuum.2024.113361.
[39] X. Liu, G.J. Ma, G. Sun, Y.P. Duan, S.H. Liu, The influence of Ti doping on the mechanical properties of TaN film, Surf. Coating. Technol. 212 (2012) 128–133, https://doi.org/10.1016/j.surfcoat.2012.09.033.
[40] Y. Wang, X. Shi, M. Liu, Y. Yang, Q. Gao, B. Zhu, L. Xu, Structure and properties of Ta doped TiN films prepared using different sputtering powers for Ta target, PAC 16 (2022) 191–200, https://doi.org/10.2298/PAC2203191W.
[41] D.K. Jiao, X.F. Luo, Y.P. Hou, Y.Y. Zhang, D. Hao, Research on the durability degradation evaluation method of metal bipolar plate for proton exchange membrane fuel cells, Chinese Battery Industry. https://link.cnki.net/urlid/32.1448, 2024.
[42] A. Kumar, M. Ricketts, S. Hirano, Ex situ evaluation of nanometer range gold coating on stainless steel substrate for automotive polymer electrolyte membrane fuel cell bipolar plate, J. Power Sources 195 (2010) 1401–1407, https://doi.org/10.1016/j.jpowsour.2009.09.022.
[43] G.M. Matenoglou, ChE. Lekka, L.E. Koutsokeras, G. Karras, C. Kosmidis, G. A. Evangelakis, P. Patsalas, Structure and electronic properties of conducting, ternary $Ti_xTa_{1-x}N$ films, J. Appl. Phys. 105 (2009) 103714, https://doi.org/10.1063/1.3131824.
[44] G. Abadias, L.E. Koutsokeras, Ph Guerin, P. Patsalas, Stress evolution in magnetron sputtered Ti-Zr-N and Ti-Ta-N films studied by in situ wafer curvature: role of energetic particles, Thin Solid Films 518 (2009) 1532–1537, https://doi.org/10.1016/j.tsf.2009.07.183.
[45] L. Zhu, J. He, D. Yan, Synthesis and microstructure observation of titanium carbonitride nanostructured coatings using reactive plasma spraying in atmosphere, Appl. Surf. Sci. 257 (2011) 8722–8727.
[46] Y. Zhao, G. Lin, J. Xiao, TiN/TiC multilayer films deposited by pulse biased arc ion plating, Vacuum 85 (2010) 1–4, https://doi.org/10.1016/j.vacuum.2009.04.043.
[47] M.S. Kabir, P. Munroe, Z.F. Zhou, Z.H. Xie, Structure and mechanical properties of graded Cr/CrN/CrTiN coatings synthesized by close field unbalanced magnetron sputtering, Surf. Coating. Technol. 309 (2017) 779–789, https://doi.org/10.1016/j.surfcoat.2016.10.087.
[48] E. Niu, L. Li, G. Lv, W. Feng, H. Chen, S. Fan, S. Yang, X. Yang, Synthesis and characterization of tantalum nitride films prepared by cathodic vacuum arc technique, Appl. Surf. Sci. 253 (2007) 5223–5227, https://doi.org/10.1016/j.apsusc.2006.11.042.
[49] A.C. Hee, Y. Zhao, S.S. Jamali, A. Bendavid, P.J. Martin, H. Guo, Characterization of tantalum and tantalum nitride films on Ti6Al4V substrate prepared by filtered cathodic vacuum arc deposition for biomedical applications, Surf. Coating. Technol. 365 (2019) 24–32, https://doi.org/10.1016/j.surfcoat.2018.05.007.
[50] T. Li, Z. Yan, Z. Liu, M. He, Y. Yan, Y. Chen, High corrosion resistance and surface conductivity of $(Ti_{1-x}Cr)N$ coating for titanium bipolar plate, Corrosion Sci 200 (2022) 110256, https://doi.org/10.1016/j.corsci.2022.110256.
[51] X.Z. Wang, M.M. Zhang, Q. Hu, S. Su, H.Q. Fan, H. Wang, J.L. Luo, Optimizing the interfacial potential distribution to mitigate high transient potential induced dissolution on C/Ti coated metal bipolar plates used in PEMFCs, Corrosion Sci. 208 (2022) 110686, https://doi.org/10.1016/j.corsci.2022.110686.
[52] L. Zhang, L. Qi, S. Deng, O. Oguntuase, T. Deng, H. Wang, O.A. Ojo, Analyses of anodically formed passive film and corrosion behavior of wire-arc additive manufactured ATI 718 Plus® superalloy, Addit. Manuf. 48 (2021) 102443, https://doi.org/10.1016/j.addma.2021.102443.
[53] O. Sharifahmadian, A. Pakseresht, K.K. Amirtharaj Mosas, D. Galusek, Doping effects on the tribological performance of diamond-like carbon coatings: a review, J. Mater. Res. Technol. 27 (2023) 7748–7765, https://doi.org/10.1016/j.jmrt.2023.11.132.
[54] I. Ferreri, M. Henriques, J.T.M. De Hosson, A. Cavaleiro, S. Carvalho, Nano-galvanic coupling for enhanced Ag+ release in ZrCN-Ag films: antibacterial application, Surf. Coating. Technol. 298 (2016) 1–6, https://doi.org/10.1016/j.surfcoat.2016.04.019.
[55] P.P. Wu, G.L. Song, Y.X. Zhu, Z.L. Feng, D.J. Zheng, The corrosion of Al-supersaturated Mg matrix and the galvanic effect of secondary phase nanoparticles, Corrosion Sci. 184 (2021) 109410, https://doi.org/10.1016/j.corsci.2021.109410.
[56] L. Castanheira, M. Bedouet, A. Kucernak, G. Hinds, Influence of microporous layer on corrosion of metallic bipolar plates in fuel cells, J. Power Sources 418 (2019) 147–151, https://doi.org/10.1016/j.jpowsour.2019.02.005.
[57] S. Ren, C. Du, Z. Liu, X. Li, J. Xiong, S. Li, Effect of fluoride ions on corrosion behaviour of commercial pure titanium in artificial seawater environment, Appl. Surf. Sci. 506 (2020) 144759, https://doi.org/10.1016/j.apsusc.2019.144759.
[58] R. Li, Y. Cai, K. Wippermann, W. Lehnert, The electrochemical behavior of CrN/Cr coatings with defects on 316L stainless steel in the simulated cathodic environment of an HT-PEFC, J. Electrochem. Soc. 166 (2019) C394–C400, https://doi.org/10.1149/2.0591913jes.
[59] Y. Guo, H.P. Chen, R.Y. Li, J.T. Geng, Z.G. Shao, Nb-Cr-C coated titanium as bipolar plates for proton exchange membrane fuel cells, J. Power Sources 520 (2022) 230797, https://doi.org/10.1016/j.jpowsour.2021.230797.
[60] A. Ingle, V. Raja, J. Rangarajan, P. Mishra, Corrosion resistant quaternary Al-CrMo-N coating on type 316L stainless steel bipolar plates for proton exchange membrane fuel cells, Int. J. Hydrogen Energy 45 (2020) 3094, https://doi.org/10.1016/j.ijhydene.2019.11.119, 3017.
[61] J. Jin, Z. He, X. Zhao, Formation of a protective TiN layer by liquid phase plasma electrolytic nitridation on Ti-6Al-4V bipolar plates for PEMFC, Int. J. Hydrogen Energy 45 (2020) 12489–12500, https://doi.org/10.1016/j.ijhydene.2020.02.152.
[62] L. Wang, D.O. Northwood, X. Nie, J. Housden, E. Spain, A. Leyland, A. Matthews, Corrosion properties and contact resistance of TiN, TiAlN and CrN coatings in simulated proton exchange membrane fuel cell environments, J. Power Sources 195 (2010) 3814–3821, https://doi.org/10.1016/j.jpowsour.2009.12.127.
[63] J. Jin, X. Kou, X. Tian, Y. Tao, X. Xu, H. Yang, Y. Mi, Investigation of corrosion protection with conductive chromium-aluminum carbonitride coating on metallic bipolar plates, Vacuum 213 (2023) 112084, https://doi.org/10.1016/j.vacuum.2023.112084.
[64] L. Mølmen, L. Fast, A. Lundblad, P. Eriksson, P. Leisner, Contact resistance measurement methods for PEM fuel cell bipolar plates and power terminals, J. Power Sources 555 (2023) 232341, https://doi.org/10.1016/j.jpowsour.2022.232341.
[65] B.B. Burton, A.R. Lavoie, S.M. George, Tantalum nitride atomic layer deposition using (tert-butylimido) tris (diethylamido) tantalum and hydrazine, J. Electrochem. Soc. 155 (7) (2008) D508–D516, https://doi.org/10.1149/1.2908741.
[66] M. Chen, J.C. Ding, S.H. Kwon, Q. Wang, S. Zhang, Corrosion resistance and conductivity of NbN-coated 316L stainless steel bipolar plates for proton exchange membrane fuel cells, Corrosion Sci. Mar 196 (2022) 110042, https://doi.org/10.1016/J.CORSCI.2021.110042.
[67] M. Atapour, V. Rajaei, S. Trasatti, M.P. Casaletto, G.L. Chiarello, Thin niobium and niobium nitride PVD coatings on AISI 304 stainless steel as bipolar plates for PEMFCs, Coatings Sep 10 (9) (2020) 889, https://doi.org/10.3390/coatings10090889.
[68] S. Mirhashemihaghighi, J. Swiatowska, V. Maurice, A. Seyeux, S. Zanna, E. Salmi, M. Ritala, P. Marcusa, Corrosion protection of aluminium by ultra-thin atomic layer deposited alumina coatings, Corrosion Sci 106 (2016) 16–24, https://doi.org/10.1016/j.corsci.2016.01.021.
[69] S. Jannat, H. Rashtchi, M. Atapour, M.A. Golozar, H. Elmkhah, M. Zhiani, Preparation and performance of nanometric Ti/TiN multi-layer physical vapor deposited coating on 316L stainless steel as bipolar plate for proton exchange membrane fuel cells, J. Power Sources 435 (30) (2019) 226818, https://doi.org/10.1016/j.jpowsour.2019.226818.
[70] K. Feng, Z. Li, H. Sun, L. Yu, X. Cai, Y. Wu, P.K. Chu, C/CrN multilayer coating for polymer electrolyte membrane fuel cell metallic bipolar plates, J. Power Sources 222 (15) (2013) 351–358, https://doi.org/10.1016/j.jpowsour.2012.08.087.
[71] J. Jin, Z. Zhu, D. Zheng, Influence of Ti content on the corrosion properties and contact resistance of CrTiN coating in simulated proton exchange membrane fuel cells, Int. J. Hydrogen Energy 42 (16) (2017) 11758–11770, https://doi.org/10.1016/j.ijhydene.2017.02.014.
[72] S.H. Lee, N. Kakati, J. Maiti, S.H. Jee, D.J. Kalita, Y.S. Yoon, Corrosion and electrical properties of CrN- and TiN-coated 316L stainless steel used as bipolar plates for polymer electrolyte membrane fuel cells, Thin Solid Films 529 (2013) 374–379, https://doi.org/10.1016/j.tsf.2012.09.027.
[73] T. Li, H. Zhang, Y. Wang, C. Wu, Y. Yan, Y. Chen, TiCr transition layer promoting the growth of high-stability TiCrN coating for titanium bipolar plate, Surf. Coating. Technol. 451 (2022) 129026, https://doi.org/10.1016/j.surfcoat.2022.129026.
[74] L. Chen, R. Liu, B. Zhang, J. Lv, J. Zhang, Nano-Cr_2N dominated films with high conductivity and strong corrosion resistance for Ti bipolar plates, Mater. Des. 224 (2022) 111305, https://doi.org/10.1016/j.matdes.2022.111305.
[75] S. Pugal Mani, M. Kalaiarasan, K. Ravichandran, N. Rajendran, Y. Meng, Corrosion resistant and conductive TiN/TiAlN multilayer coating on 316L SS: a promising metallic bipolar plate for proton exchange membrane fuel cell, J. Mater. Sci. 56 (2021) 10575–10596, https://doi.org/10.1007/s10853-020-05682-4.
[76] L. Mendizabal, A. Oedegaard, O.E. Kongstein, S. Lædre, J. Walmsley, J. Barriga, J. J. Gonzalez, TaN_X coatings deposited by HPPMS on SS316L bipolar plates for polymer electrolyte membrane fuel cells: correlation between corrosion current,

contact resistance and barrier oxide film formation, Int. J. Hydrogen Energy 42 (5) (2017) 3259–3270.